Science of the Total Environment 905 (2023) 167203

Contents lists available at ScienceDirect

Science of the Total Environment

journal homepage: www.elsevier.com/locate/scitotenv

Remotely sensed evidence of the divergent climate impacts of wind farms on croplands and grasslands

Naijing Liu[a,b,c], Xiang Zhao[a,b,*], Xin Zhang[d], Jiacheng Zhao[a,b], Haoyu Wang[e], Donghai Wu[f,*]

[a] State Key Laboratory of Remote Sensing Science, Faculty of Geographical Science, Beijing Normal University, Beijing 100875, China
[b] Beijing Engineering Research Center for Global Land Remote Sensing Products, Faculty of Geographical Science, Beijing Normal University, Beijing 100875, China
[c] POWERCHINA Northwest Engineering Corporation Limited, Xi'an, Shaanxi 710065, China
[d] School of Computing, Mathematics and Digital Technology, Manchester Metropolitan University, Manchester M1 5GD, UK
[e] School of Earth and Space Sciences, Peking University, Beijing 100871, China
[f] Key Laboratory of Vegetation Restoration and Management of Degraded Ecosystems, Guangdong Provincial Key Laboratory of Applied Botany, South China Botanical Garden, Chinese Academy of Sciences, Guangzhou 510650, China

HIGHLIGHTS

- Wind farms lead to warming and cooling effects on grassland and cropland, separately.
- Irrigation results in more obvious cooling effects on cropland wind farms.
- Climate and terrain factors can explain the surface temperature changes of wind farms.

GRAPHICAL ABSTRACT

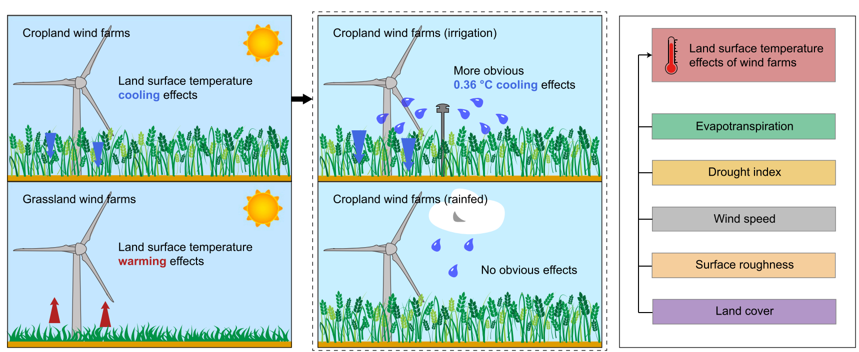

ARTICLE INFO

Editor: Elena Paoletti

Keywords:
Land surface temperature
Heterogeneity
Remote sensing
Wind farm
Grassland
Cropland

ABSTRACT

To mitigate climate change, the utilization of wind energy has rapidly expanded over the last two decades. However, when producing clean electricity, wind farms (WFs) may in turn alter the local climate by interfering in land surface-atmosphere interactions. Currently, China and the United States have the highest wind energy capacities globally. Thus, quantitatively analyzing the impacts of WFs on land surface temperature (LST) between the two countries is valuable to deeply understand the climate impact of WF. In this study, we use the moderate-resolution imaging spectroradiometer (MODIS) time series from 2001 to 2018 to reveal the impacts of 186 WFs (76 in China and 110 in the US) on local LSTs. The remote sensing observations reveal that WFs generally lead to warming impacts in both countries, with stronger effects in the US compared to China. During the daytime, WFs in the US exhibit a significant warming effect of 0.08 °C ($p < 0.05$), while the impact in China is nonsignificant (0.06 °C, $p = 0.15$). At night, the warming impacts in the US are approximately 1.7 times greater than in China (0.19 °C vs. 0.11 °C). Differences in the LST impacts between the two countries are primarily driven by cropland WFs, which cause more significant cooling effects in China (−0.34 °C in the daytime and −0.19 °C at night, $p < 0.01$) compared to the US. However, these differences are not significant for grassland WFs.

* Corresponding authors.
E-mail addresses: zhaoxiang@bnu.edu.cn (X. Zhao), donghaiwu@scbg.ac.cn (D. Wu).

https://doi.org/10.1016/j.scitotenv.2023.167203
Received 14 July 2023; Received in revised form 9 September 2023; Accepted 17 September 2023
Available online 18 September 2023
0048-9697/

Moreover, the impacts of WFs on croplands' LSTs are strongly correlated with their evapotranspiration impacts, likely influenced by irrigation practices. In addition to evapotranspiration, a machine learning model suggests that background climate and terrain factors can alter the LST impacts. Our observations in the two largest WF-deployment countries provide a new understanding of the climate impacts of WFs, which should be considered in the fields of wind and renewable energy deployment.

1. Introduction

In attempts to confront the global warming induced by fossil fuel consumption, the world wind energy capacity has been exploding since the beginning of the 21st century (Veers et al., 2019). According to the World Wind Energy Association, global wind energy production could support 6 % of the total electricity consumption with a capacity of 597 gigawatts by the end of 2018 (World Wind Energy Association, 2019). From a prospective view, the wind energy capacity must keep growing by 18 % per year between 2020 and 2030 due to the increasing total electricity demand and the goal of net-zero emissions (International Energy Agency, 2021).

However, when producing clean electricity, wind farms (WFs) impact the local climate (Dai et al., 2015; Tabassum-Abbasi et al., 2014; Wang and Wang, 2015). The rotation blades of turbines generate wake turbulence, which can interfere with the vertical heat flux of the atmospheric boundary layer (ABL) and, further, the land surface temperature (LST) (Armstrong et al., 2014; Roy and Traiteur, 2010). Based on remotely sensed observations, WFs lead to significant warming effects on local LSTs in the nighttime (Liu et al., 2022; Slawsky et al., 2015; Tang et al., 2017; Wu et al., 2019; Zhou et al., 2013; Zhou et al., 2012) and have divergent LST impacts in the daytime (Slawsky et al., 2015; Tang et al., 2017; Wu et al., 2019; Zhou et al., 2013; Zhou et al., 2012; Qin et al., 2022). Model simulations performed in various regions have also shown warming effects of WFs with magnitudes of 0.2–2.16 °C at different scales (Keith et al., 2004; Li et al., 2018; Miller and Keith, 2018; Pryor et al., 2018; Vautard et al., 2014; Xia et al., 2017).

In China and the United States, the accumulated wind energy capacities ranked first and second worldwide in 2018, at 217 and 96 Gigawatts, respectively, providing 36.3 % and 16.1 % of the world's total capacity (World Wind Energy Association, 2019). The distribution of wind energy in China and the United States is spread over typical climate and land cover types in the northern hemisphere (Ljungqvist et al., 2012; Sun et al., 2018), thus, quantitative analysis of the differences and similarities WF impacts on LSTs on surface temperature (LST) in the two countries is of great significance to understand the impact of WF in the northern hemisphere. Besides, the WFs in the two countries are located mainly in grassland and cropland regions (Rand et al., 2020; Zhang et al., 2020), and the differences in WF LST impacts should be analyzed separately for these two land cover types. For example, although both land types are covered by annual plants, croplands experience much higher human management levels than grasslands, which might lead to high uncertainties when performing driving factor analyses of mixed land-cover types. In addition, the heterogeneities introduced by the climate background and other factors should be further discussed in both China and the US.

Thus, in this study, we use 186 large cropland and grassland WFs in China and in the US to reveal the similarities and differences between these countries as well as the possible driving mechanisms of the impacts of WFs on LSTs in these two countries. By using remote sensing time series, we calculate the WF impacts on daytime and nighttime LSTs during the growing season (April to October) in China and the US. Then, these impacts are evaluated separately for cropland and grassland WFs. Finally, we explore the possible driving mechanisms of the LST impacts and the corresponding driving factors using linear regression and machine learning modeling.

2. Materials and methods

2.1. Study area

In this study, we extract 25,139 wind turbines in 76 WFs in China in 2018 by using the deep learning algorithm You Only Look Once (YOLO); these WFs are located mainly in Inner Mongolia and on the Loess Plateau, Northeast Plain, and Shandong Peninsula (Zhang et al., 2020). YOLO is an effective and precise object-detection approach based on a single neural network (Redmon et al., 2016). We also withdraw 24,513 wind turbines in 110 WFs from the US Wind Turbines Dataset; these WFs are located mainly on the Great and Central Plains (Rand et al., 2020). To facilitate a comparison with the WFs extracted in China in 2018, wind turbines constructed before 2019 in the US are selected. Among these WFs, 16 cropland WFs contain 4252 turbines in China, while 11,701 turbines are present in 54 cropland WFs in the US. For grasslands, 60 WFs contain 20,887 turbines in China, and 56 WFs have 12,812 turbines in the US.

Comparing WF pixels with their surrounding control region (buffer) is a widely used strategy for detecting WF impacts (Slawsky et al., 2015; Zhou et al., 2012; Qin et al., 2022). To ensure that every wind turbine is included, in this study, the WF areas are extracted as 1-km × 1-km pixels that contain at least one turbine. To ensure that the buffer areas share a similar climate background with the WF areas and prevent wind turbine ABL turbulence, the buffer is built in 1-km × 1-km pixels 5 to 10 km outside the WF (Tang et al., 2017; Zhou et al., 2020). The distance between adjacent wind turbines within the same WF should not be longer than 5 km. In cropland or grassland WFs, the cropland or grassland pixels are finally filtered by Moderate Resolution Imaging Spectroradiometer (MODIS) MCD12Q1 International Geosphere-Biosphere Programme (IGBP) land cover data in the WF and buffer areas, and the filtered pixels are defined as wind farm pixels (WFPs) and buffer pixels (BUPs) in the following text. To better illustrate the build processes of WFPs and BUPs, the steps are shown in Fig. S1.

2.2. Datasets

To reveal the cropland and grassland WF impacts on the local LSTs, we use the MODIS MOD11A2 land surface temperature (LST) time series recorded between 2001 and 2018. The MODIS LST product contains both daytime (10:30 AM) and nighttime (10:30 PM) bands with temporal and spatial resolutions of 8 days and 1 km (Wan et al., 2015).

To understand the possible mechanisms between the LST impacts and related environmental factors while considering heat transfer processes such as convection and phase transitions, we use five types of factors in this study, including climate, terrain, size, vegetation, and shape factors. For climate factors, we use European Centre for Medium-Range Weather Forecasts Reanalysis v5 (ERA5) precipitation, air temperature at 2-m aboveground, wind speed at 100-m aboveground (Muñoz-Sabater et al., 2021), and drought index data. This product is an hourly dataset with a spatial resolution of 0.25°. The wind speed at 100 m is selected because this layer is close to the height of wind turbines. We calculate the drought index by obtaining the ratio of ERA5 precipitation and MOD16A2 potential evapotranspiration (Running et al., 2017). We use the Köppen-Geiger climate classification to identify the climate zone of the WFs. The data has a spatial resolution of 0.0083° (Beck et al., 2018).

The terrain factors include the elevation and surface roughness. The elevation data are obtained from the Shuttle Radar Topography Mission (SRTM) DEM dataset, with a spatial resolution of 90 m (Jarvis et al., 2008). We select the Sentinel-1 Synthetic Aperture Radar (SAR) Ground Range Detected (GRD) dataset as the surface roughness indicator; it is a daily dataset with a spatial resolution of 10 m (Torres et al., 2012). The size factors are derived from wind turbines and pixels within WFPs, including the number, area, and density of turbines as well as the base of the natural logarithm of wind turbines (ln(WTs)). The area is the number of 1-km × 1-km WF pixels, and the density is the ratio of the turbines and area. The vegetation factors include the MODIS evapotranspiration, normalized difference vegetation index (NDVI), and the Global Food Security-support Analysis Data (GFSAD) irrigation dataset. The MOD16A2 evapotranspiration is an accumulated 8-day product with a spatial resolution of 500 m (Running et al., 2017; Running et al., 2015), while MOD13A1 NDVI is composited for 16 days at the same spatial resolution (Didan, 2015; Running and Zhao, 2019). The GFSAD dataset is used to indicate irrigation areas within the cropland WFs; the spatial resolution of this dataset is 1 km, and it represents the irrigation strength in 2010 (Teluguntla et al., 2015). Accumulative factors such as precipitation and evapotranspiration are accumulated in each growing-season period to match the growing-season ΔLST. Factors representing surface properties such as surface roughness are calculated by the mean growing-season value. Moreover, instantaneous factors such as the air temperature and wind speed are calculated separately for daytime and nighttime.

The shape factors describe the distribution of wind turbines within the WFs in different dimensions, including the patch density, Euclidean's nearest-neighbor distance, and shape index; these factors are calculated via the Fragstates platform (version 4.2.1) (McGarigal, 1995) as follows:

$$PD_i = \frac{N_i}{a_i} * 100 * 10000 \tag{1}$$

$$ENN_i = \frac{\sum_{j=1}^{n} h_{ij}}{n} \tag{2}$$

$$SI_i = \frac{0.25 * p_i}{\sqrt{a_i}} \tag{3}$$

where PD_i, ENN_i, and SI_i are the patch density, mean Euclidean nearest-neighbor distance, and shape index of WF i, respectively; N_i is the number of patches in the WF; n is the number of patch pairs of WFs; h_{ij} is the distance to the nearest neighboring patch (m); p_i is the perimeter of the WF (m); and a_i is the area of the WF (m^2). The patch of patch density is determined from an independent group of WF pixels using the 8-neighbor rule in our study. This term indicates the number of patches within 100 ha and increases when more fragments are present in a WF. The mean Euclidean nearest-neighbor distance increases when the adjacent fragments become farther apart. In addition, the shape index usually increases as the fragments become more irregular and split.

2.3. Assessment of wind farm impacts

The LST difference between the WFPs and BUPs could be regarded as the impact of WFs because these two regions are distributed 5 km from each other and share similar background climate conditions. The major difference between these two areas is the presence or absence of a WF. The ΔLST value is calculated by obtaining the slope of the LST difference time series in each WF, and the time series is built as follows (Qin et al., 2022; Zhou et al., 2020):

$$\Delta LST_{i \bullet j} = LST_{WFPs \bullet i \bullet j} - LST_{BUPs \bullet i \bullet j} \tag{4}$$

where $LST_{WFPs \bullet i \bullet j}$ and $LST_{BUPs \bullet i \bullet j}$ are the mean growing-season LSTs in the WFPs and the BUPs in year j, respectively; i is the serial number of the WF; and $\Delta LST_{i \bullet j}$ is the LST difference between the WFPs and BUPs. The time series of the $\Delta LST_{i \bullet j}$ values are set up in the growing season (April to October) between 2001 and 2018 through the Google Earth Engine platform (Gorelick et al., 2017). The slope of the time series is calculated by the ordinary least squares method, and the significance of the slope is tested at the 0.05 significance level. The WF impacts on LST (ΔLST) between 2001 and 2018 are calculated by multiplying the slope by the period length of 18 years. Similar to ΔLST, the differences in MODIS vegetation driving factors between the WFPs and BUPs are also calculated and expressed in uppercase Δ (e.g., Δevapotranspiration). The differences in terrain factors are calculated directly by subtracting the BUP average from the WFP average and expressed in lowercase δ (e.g., δDEM).

After configuring the growing-season daytime and nighttime ΔLSTs corresponding to each WF in this study, we also calculate the cropland and grassland WF ΔLSTs in China and the US separately. The growing season is divided into three segments: April and May, June to August, and September and October.

The ΔLSTs of concentrated and scattered WFs are also calculated to figure out the sensitivity of ΔLST on WF spatial distribution. The concentrated WFs are centralized distributed WFs located on the Great and Central Plains in the US and the southwest-northeast direction farming-pastoral ecotone in China, while the scattered WFs are the individually distributed WFs in the two countries. To explore WF-induced ΔLST in different climate zones, we divide the WFs into groups based on Köppen-Geiger climate classification. The groups with sufficient grassland and cropland WF samples are calculated. To explore the relationship between turbine density and ΔLST, we separate WFPs of each WF into pixel groups with various turbine densities, and subsequently computed their corresponding ΔLST.

2.4. Driving factor analysis

Based on a priori knowledge, to explore the main factors driving the heterogeneities in the daytime and nighttime ΔLSTs in cropland and grassland WFs in China and the US, we build linear relationships between the ΔLST values and potential continuous driving factors, including the climate, terrain, size, vegetation, and shape factors (described in 2.2). After these correlations are calculated, the significances are tested at the 0.05 significance level. To explore how wind turbine properties affect ΔLST of WFs, we analyze the linear relationships between the properties (hub height, rotor diameter, and rated power) and ΔLST based on US Wind Turbines Dataset (Rand et al., 2020; Fitch et al., 2013). The hub height, rotor diameter, and rated power of each WF is the average value of all wind turbines within the WF. However, the turbines in Northern China are extracted by deep learning algorithm (Zhang et al., 2020), there are no manufacturer information or open-access datasets of turbine properties. Thus, the related analysis are only conducted in the US. Then, to determine the main driving mechanisms of the ΔLSTs in China and the US, we build an optimal boosted regression tree model and calculate the relative importance and partial dependences of the five types of continuous factors and two categorical factors (land cover type and country) using R programming (Freund and Schapire, 1997).

3. Results

3.1. Wind farm impacts on the land surface temperature

Based on the MODIS LST time series from 2001 to 2018 characterizing the 186 WFs in China and the US, the results suggest that the average growing-season ΔLST between the WFPs and BUPs increased significantly at night for both China and the US at the $p < 0.05$ level (Fig. 1(f)). However, this magnitude is approximately 1.7 times stronger in the US than in China (0.191 °C to 0.111 °C). The average ΔLSTs in the

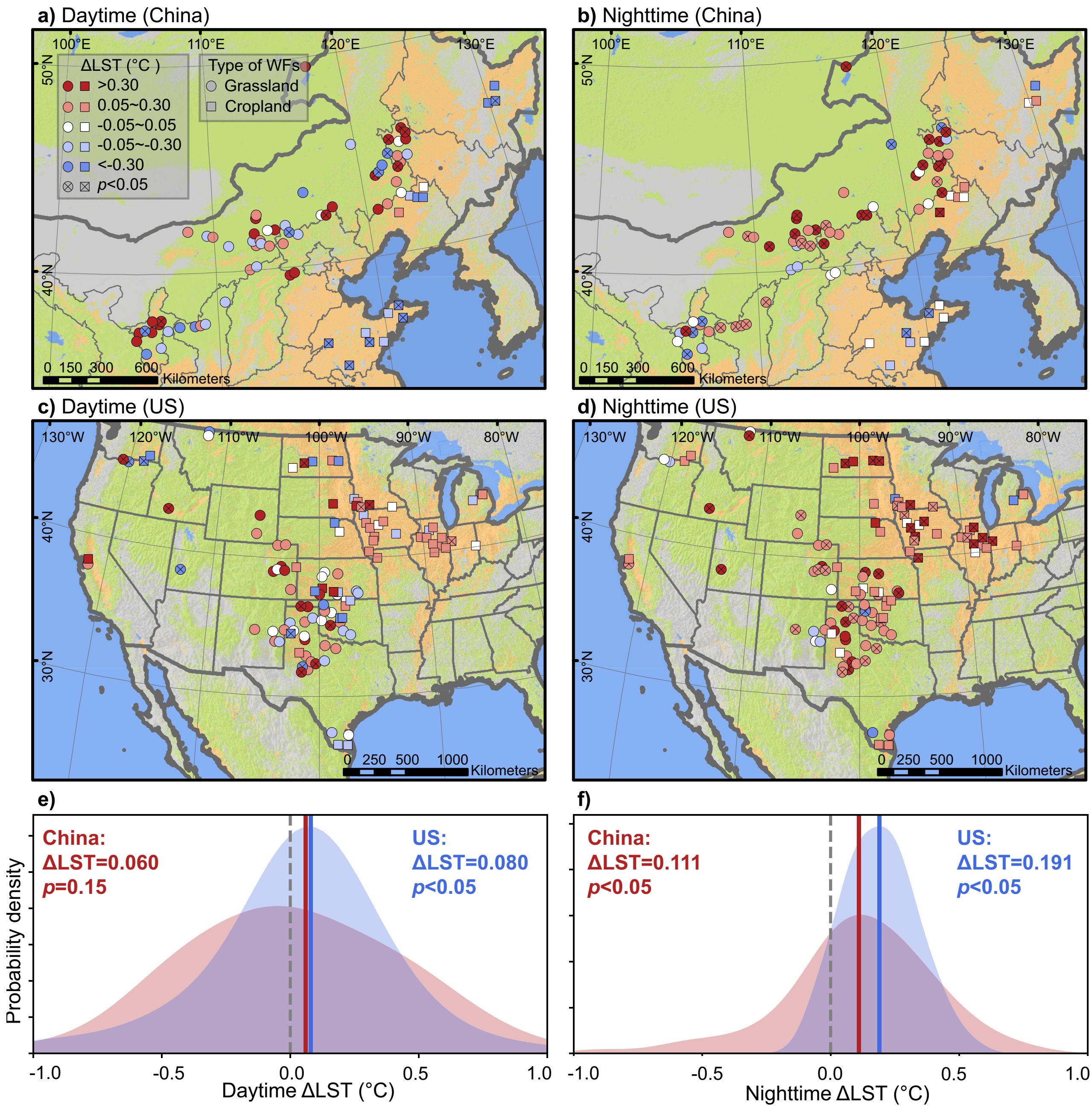

Fig. 1. MODIS growing-season daytime and nighttime time-series ΔLSTs between WFPs and BUPs at 186 WFs in China and the US from 2001 to 2018. (a), (c) Spatial distributions of daytime ΔLSTs resulting from WFs in China and the US. (b), (d) Spatial distributions of nighttime ΔLSTs resulting from WFs in China and the US. The ΔLSTs and significance of the ΔLST trends are given by symbol colors and textures. The circle and rectangle symbols represent grassland and cropland WFs, respectively. The cross symbols within the circles and rectangles indicate significant ΔLSTs at $p < 0.05$. The base maps are the MODIS MCD12Q1 International Geosphere-Biosphere Programme (IGBP) land cover classifications in 2018 with the standard colormap (green for grasslands and brown for croplands). (e), (f) Distributions of daytime and nighttime ΔLSTs resulting from WFs in China and the US. The averaged ΔLST values and the significance levels of the one-sample *t*-tests are given.

daytime non-significantly and significantly increased in China and the US (0.060 °C and 0.080 °C), respectively, as shown in Fig. 1(e). These results suggest that there are spatial and temporal differences in the impacts of WFs on local LSTs. The WF ΔLST is higher in the nighttime than in the daytime in both countries and is higher in the US than in China both in the daytime and nighttime (by 0.020 °C and 0.080 °C (33 % and 72 %), respectively) at the significance levels of $p = 0.39$ and $p < 0.05$, respectively.

In the daytime, 64.55 % of the WFs show warming impacts in the US, and 10.00 % are significant ($p < 0.05$), while 35.45 % of the WFs show cooling effects (5.45 % of which are significant). The ΔLST resulting from WFs ranges between −1.043 °C and 3.222 °C. However, in China, 51.32 % of the WFs suggest warming impacts on the LST, while the remaining WFs show cooling effects (11.84 % and 13.16 % correspond to significant warming and cooling, respectively). The ΔLST ranges from −1.125 °C to 1.915 °C. Fig. 1 (a) shows that the cropland WFs on the Northeast Plains and Shandong Peninsula of China show cooling impacts on ΔLST. At night, more WFs show warming effects in both the US and China. Specifically, in the US, 90.91 % of WFs show warming effects (40.00 % of which are significant). The nighttime ΔLST range is between −0.123 °C and 0.574 °C. Moreover, in China, 72.37 % of WFs suggest warming impacts, 38.16 % of which are significant. The nighttime ΔLST range in China is between −0.901 °C and 0.754 °C.

3.2. Divergent impacts of cropland and grassland wind farms

To determine the reason for ΔLST differences between China and the US, we also analyzed the WF-induced ΔLSTs in cropland and grassland regions separately. In the daytime, significant (−0.311 °C) cooling effects are observed to result from cropland WFs in China at $p < 0.05$, while the warming effects are nonsignificant, at 0.026 °C, in the US (Fig. 2(a)). In addition, at night, the averaged ΔLST is also higher for the US cropland WFs (0.186 °C, $p < 0.05$) than in China (−0.004 °C, $p = 0.47$) (Fig. 2(b)).

For grassland WFs, the ΔLST values are similar between China and the US. The daytime ΔLSTs increase significantly in both countries by 0.158 °C to 0.131 °C at $p < 0.05$, with values of 0.141 °C and 0.195 °C in the nighttime (Fig. 2(c), 2(d)). In summary, the ΔLST differences in cropland WFs are −0.337 °C and − 0.190 °C between the two countries in the daytime and nighttime, while the differences are 0.027 °C and -0.054 °C in grassland WFs (China minus the US). Thus, the contribution of cropland WFs to the growing-season ΔLST differences between the two countries is much higher than that of grassland WFs.

3.3. Attributions on wind farm impacts

To determine the reason for the ΔLST heterogeneities observed in the cropland WFs between the two countries, we perform linear regression between multiple driving factors and the cropland WF-induced ΔLSTs in China and the US. The daytime ΔLSTs are more strongly related to the Δevapotranspiration values in China ($r = -0.58$) than in the US ($r = -0.31$) (Fig. 3(a)). The average Δevapotranspiration value is 13.46 mm higher in China than in the US, while the daytime and nighttime ΔLSTs are 0.34 °C and 0.19 °C lower in cropland WFs in China than in the US. These ΔLST heterogeneities in the cropland WFs in the two countries might be driven by the cooling effects of evapotranspiration. Moreover, the proportion of irrigated croplands within China's (72 %) cropland WFs is much higher than that in the US (15 %) (Fig. 3(b)). Significantly higher and lower Δevapotranspiration and ΔLST values are observed in irrigated WFs than in rainfed WFs ($p < 0.05$) (Fig. 3(c), (d)). These evapotranspiration differences in cropland WFs between the two countries may be caused by agricultural human management.

To explore the relative importance levels and partial effects of the Δevapotranspiration and other related driving factors on the growing-season daytime ΔLSTs, we build a boosted regression tree model. The model can explain the ΔLST with a cross-validation correlation coefficient of 0.51. ΔEvapotranspiration is the most important driving factor affecting ΔLST, with a relative contribution of 35.7 %, while drought index, wind speed, and δsurface roughness contribute approximately 20 %, separately (Fig. 4(b-d)). The land cover factor could explain 4.6 % of ΔLST. Among these factors, the Δevapotranspiration, drought index, and δsurface roughness negatively affect ΔLST, while the wind speed

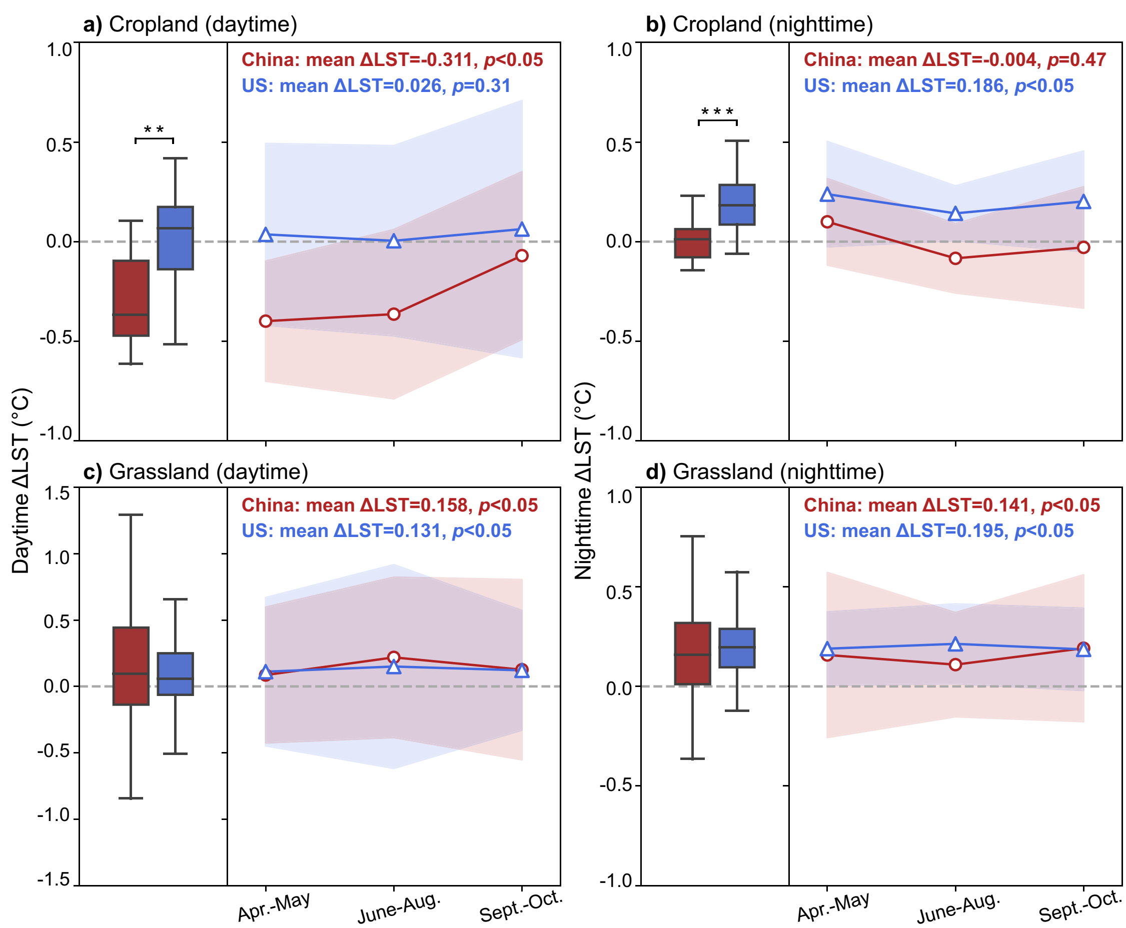

Fig. 2. Boxplots of growing-season WF-induced ΔLSTs between WFPs and BUPs and growing-season time series representing croplands and grasslands in China and the US from 2001 to 2018. Boxplots and time series of cropland WFs in a) daytime and b) nighttime are shown. Boxplots and time series of grassland WFs in c) daytime and d) nighttime are shown. The boxes and time series with red and blue colors represent ΔLSTs in China and the US, respectively. The averaged ΔLST values and the significance levels of the one-sample *t*-tests are given in the text. The significance levels of the two-sample t-tests for the WF-induced ΔLSTs between China and the US are given in asterisks with different levels (* for $p < 0.05$, ** for $p < 0.01$, and *** for $p < 0.001$). The growing season includes three periods: April and May, June to August, and September and October.

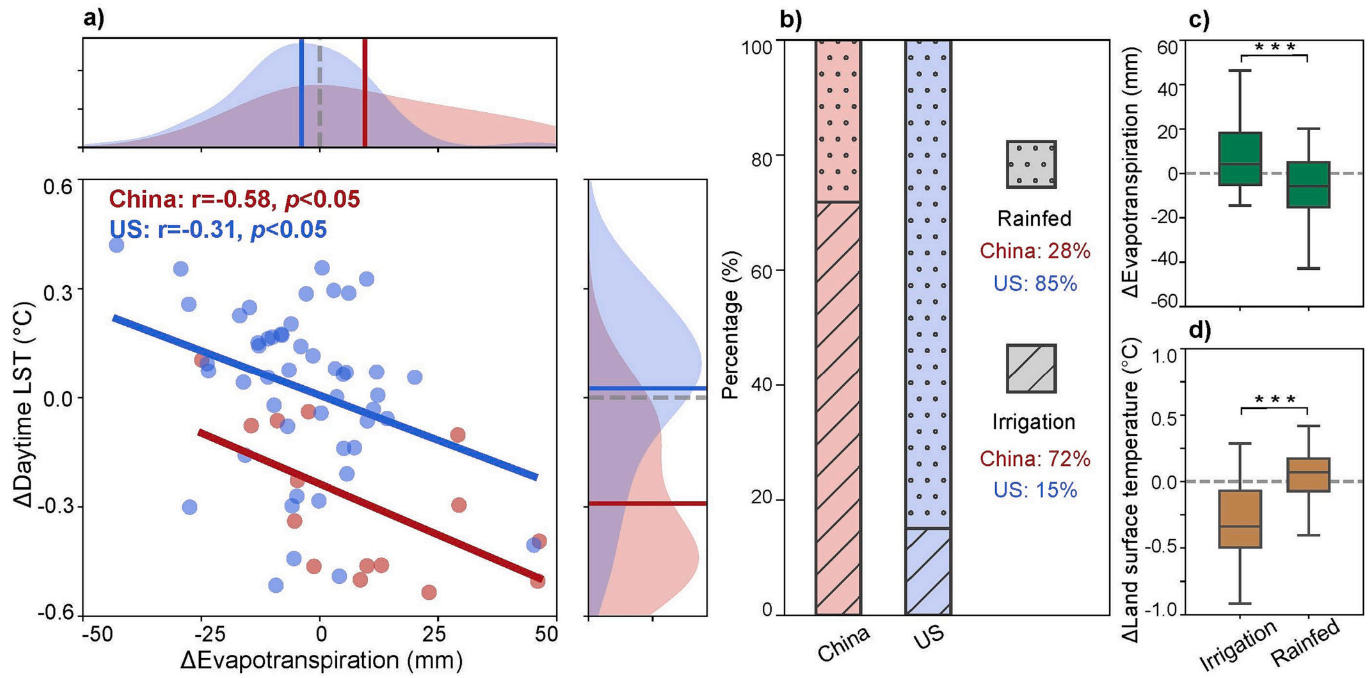

Fig. 3. Correlations between growing-season Δevapotranspiration and daytime ΔLST, the irrigation percentages, and the difference in Δevapotranspiration and ΔLST of irrigation groups on cropland WFs in China and the US. a) Correlation between Δevapotranspiration and ΔLST in China and the US. The distributions of Δevapotranspiration and ΔLST in the two countries are shown in the top and right subfigures, respectively. The correlation coefficients and the significance levels are given in the text. b) Barplot of the irrigation percentage of the cropland WFs in China and the US. c) and d) The Δevapotranspiration and ΔLST values in the irrigation and rainfed WF groups in both China and the US. The significances of the WF-induced Δevapotranspiration and ΔLST confirmed in the two-sample *t*-tests between irrigated and rainfed WFs in both China and the US are given in asterisks with different levels (* for $p < 0.05$, ** for $p < 0.01$, and *** for $p < 0.001$).

makes a positive contribution to ΔLST. The negative contribution of croplands suggests that irrigation may play an important role in decreasing ΔLST by enhancing evapotranspiration (Fig. 4e).

4. Discussion

4.1. Similar effects of grassland wind farms

In the 116 grassland WFs in both China and the US, the effect of WFs on temperature is similar, and the daytime and nighttime ΔLSTs are 0.145 °C and 0.167 °C, respectively (the standard deviations are 0.534 °C and 0.244 °C, respectively). The averaged ΔLSTs are higher in the nighttime than in the daytime; nevertheless, the standard deviations are lower in the nighttime than in the daytime. These phenomena might be explained by the ABL stability of stable, neutral, and unstable. When the ABL is stable, it is likely to be a nighttime circumstance. The turbulence produced by wind turbines mixes the warmer upper air layer and the cooler layer near the surface, causing the land surface to be heated (Wu and Archer, 2021). However, in the daytime, the ABL stability can be more complicated, with stable, unstable, or neutral situations. When the ABL is unstable, the land surface can be cooled by the mixing of the cooler upper air and the warmer near-surface air. Moreover, when the ABL is neutral, the impact on the LST is near zero because of the weak heat convection between the upper and lower air layers with the approximate temperature (Qin et al., 2022; Miller and Keith, 2018; Zhou et al., 2020). Thus, the average ΔLST and standard deviation could be lower and higher, respectively, in the daytime than in the nighttime.

Considering China's desert WFs, which share the similar low human management levels to the grassland WFs in this study, the warming effects of the desert WFs are much higher than the grassland WF effects determined in this study. The desert WF-induced ΔLSTs from 2001 to 2018 are 0.250 °C and 0.237 °C in the daytime and nighttime, respectively, (Liu et al., 2022), while those of grassland WFs are 0.060 °C and 0.111 °C, respectively. The daytime and nighttime ΔLST differences between desert and grassland WFs are obvious, which might be the result of the cooling effects of plant and soil evapotranspiration (Pallas Jr et al., 1967; Seneviratne et al., 2010). However, the ΔLST ranges are higher in grassland WFs than in desert WFs. In the daytime, the grassland WF-induced ΔLSTs range from −1.125 °C to 1.915 °C, while this range is −0.729 °C to 1.456 °C for desert WFs. In addition, the ΔLST ranges are −0.901 °C to 0.754 °C and -0.033 °C to 0.543 °C for vegetated and desert WFs at night, respectively. These differences might be due to the more divergent underlying conditions in grassland areas than in desert areas. For example, the standard deviations of evapotranspiration and vegetation cover are much higher in grasslands than in deserts (De Keersmaecker et al., 2015; Jung et al., 2010), and the human activity strength variations are higher in areas covered by vegetation than in barren areas.

4.2. Divergent impacts of cropland wind farms

For the cropland WFs in China, the average ΔLST values are −0.311 °C and -0.004 °C with standard deviations of 0.210 °C and 0.167 °C in the daytime and nighttime, respectively. In comparison, the daytime and nighttime ΔLST of cropland WFs in the US are 0.026 °C and 0.186 °C in the daytime and nighttime (with standard deviations of 0.385 °C and 0.128 °C), respectively. The average daytime ΔLST in China is lower than that in the US. This might be the result of the relatively high irrigation percentage in China's cropland WFs compared to those in the US (72 % in China to 15 % in the US, Fig. 3(b)) (Kimm et al., 2020; Yin et al., 2020) of stronger irrigation activities leading to higher evapotranspiration cooling effects. Moreover, the standard deviation of the daytime ΔLST in China is also lower than that in the US, which might suggest that a high irrigation percentage leads to relatively steady cooling effects in cropland WFs (Lobell et al., 2008).

In the 70 cropland WFs in both China and the US, the averaged ΔLST values are −0.050 °C and 0.143 °C, with standard deviations of 0.380 °C and 0.159 °C, in the daytime and nighttime, respectively. Similar to

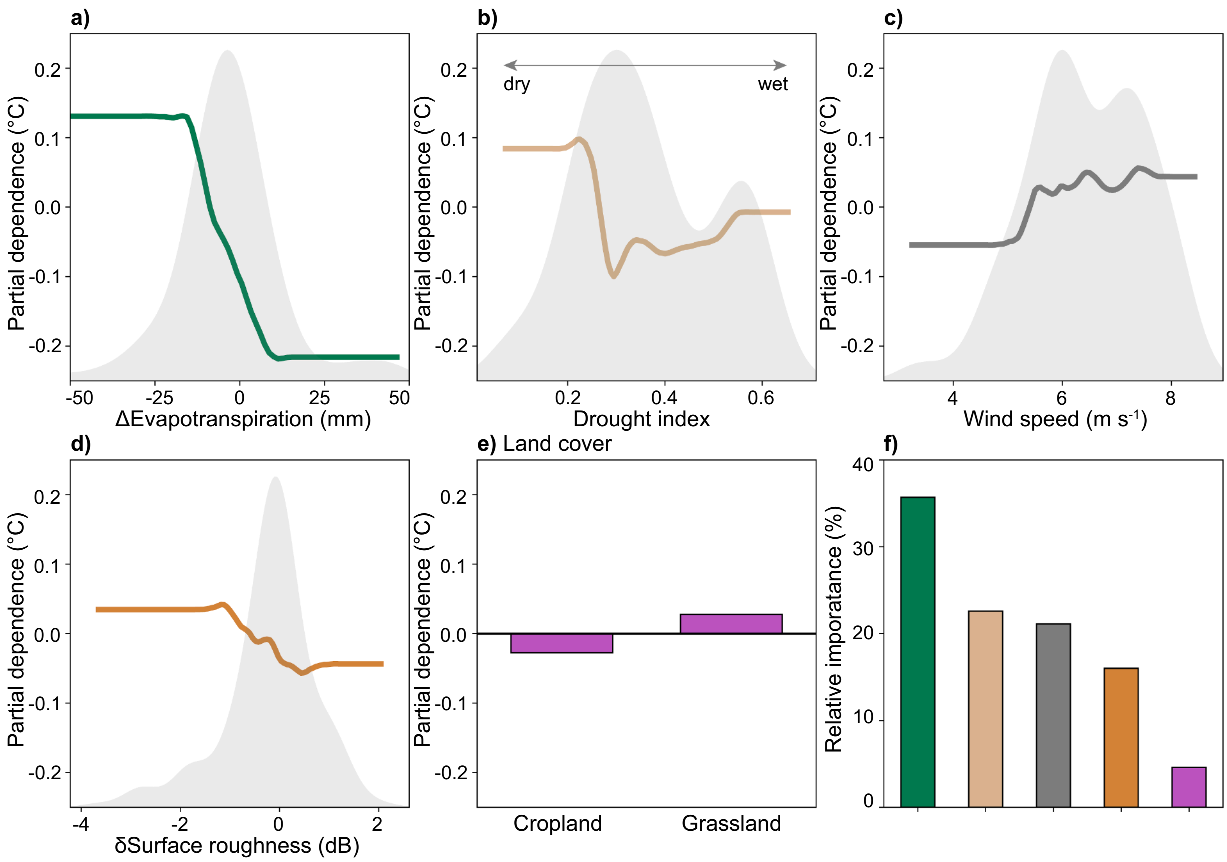

Fig. 4. Relative importance levels and partial dependences of the continuous and categorical driving factors on ΔLST in 186 WFs in both China and the US based on the boosted regression tree results. (a–e) Partial effects of different variables on ΔLST. (f) Relative contribution (%) of each variable (green for Δevapotranspiration, tan for drought index, gray for wind speed, brown for δsurface roughness, purple for land cover).

grassland WFs, the ΔLSTs are higher in the nighttime than in the daytime, while the standard deviations are lower. These differences might be explained by the ABL stability. A more stable ABL leads to higher nighttime ΔLSTs, while a more divergent daytime ABL stability brings higher standard deviations (Wu and Archer, 2021). Furthermore, although the average ΔLST is only 0.024 °C lower at night than during the daytime, the average daytime ΔLST is 0.195 °C lower in the cropland WFs than in the grassland WFs. This difference is likely caused by the relatively high evapotranspiration in cropland WFs compared to grassland WFs (Purdy et al., 2018) leading to stronger cooling effects of cropland WFs than grassland WFs. In previous studies, cropland WFs led to nighttime warming effects with magnitudes ranging from 0.26 °C to 0.31 °C, while the impacts were not obvious in the daytime (Slawsky et al., 2015; Xia et al., 2016). The impacts are similar to those found in our study.

4.3. Driving factors affecting wind farm impacts

The primary climate driving factors in affecting WF-induced LST changes are the ABL stability and the wind speed. The two factors decide the temperature gradient and the turbulence strength created by wind turbine, which further affect the local LST through heat transfer (Zhou et al., 2020; Fitch et al., 2013). Beside of that, some other factors might else have influence on the ΔLST. Fig. 4 shows that evapotranspiration is the most important driving factor during the growing season affecting the WF-induced ΔLST in both China and the US. In the daytime, the water turns from liquid to vapor through plant leaf stomata and the soil surface. During this phase change, heat is absorbed from the leaf and soil surfaces (Pallas Jr et al., 1967; Seneviratne et al., 2010). This might lead to cooling effects in high-evapotranspiration WF regions. At night, plant transpiration is lower than in the daytime. When the rotation of a turbine causes the warmer upper layer and cooler surface layer to mix, soil evaporation can suppress the warming trends of the land surface (Malek, 1992). WFs in different absolute LST zones might have various relationship between Δevapotranspiration and ΔLST, thus we calculate the linear relationship the two variables in LST groups of <27 °C and >27 °C of cropland WFs in both China and the US (Fig. S2). The results show that there are obvious negative correlation in LST group of <27 °C in the two countries ($p < 0.1$), while the negative relationship is weaker in the group of >27 °C in both countries. This could be attributed to the base evapotranspiration is higher in groups of >27 °C, and the increase of evapotranspiration lead to weaker LST effects in those WFs (He et al., 2020; Yao et al., 2017).

Apart from evapotranspiration, relatively fast wind speeds lead to increased rotation speeds of turbines until the rated power is reached (Ragheb and Ragheb, 2011); thus, the mixing effect of the ABL and land surface warming may be enhanced. The δsurface roughness values are negatively related to ΔLSTs. This might be because when the WFPs and rougher than the BUPs, the vertical and horizontal heat fluxes are increased, further strengthening surface dissipation (Oke, 1973). The higher ΔLSTs observed in drier WFs are likely related to the relatively high water stress and low water contents of these WFs. In such areas, soil evaporation is limited by the moisture content, and plants tend to close their stomata to conserve water and suppress transpiration (Osakabe et al., 2014). In relatively moist WFs, the high water contents of the leaves and soil can keep these surfaces cool (Ceccato et al., 2001).

The increase of turbine density within WFs might enhance turbulence strength and the resulting changes of ΔLST (Fitch et al., 2013). To make a quantitative analysis of this effect, we calculated the ΔLST values for pixel groups within each WF that varied in turbine density.

The results depicted in Fig. S3 indicate that there are no significant ΔLST differences among the various density groups during both daytime and nighttime. Interestingly, the ΔLST values for pixels with only one turbine are similar to those with multiple turbines. This observation may be attributed to the wake effect of turbulence generated by wind turbines, which can spread several kilometers in the downwind direction (Lundquist et al., 2019). As a result, the mixing effect created by turbines could cover several pixels in the downwind direction and obscure the ΔLST brought by turbines in those pixels.

Local heat, moisture, and human activities differ among climate zones, which might interfere with WF-induced ΔLST. We analyzed the ΔLST on cropland and grassland WFs in both countries in different climate zones based on the Köppen-Geiger classification. It is shown that the ΔLST of cropland WFs are considerably lower than grassland ones in the Dwa climate zone, while the difference is not obvious between cropland and grassland WFs in the Dfa zone (Fig. S4). This difference can be attributed to the irrigation on most cropland WFs in the Dwa zone (the irrigation proportion is 69 % in the Dwa zone while it is 5 % in the Dfa zone). The same results could be drawn as it is in Section 3.3 that irrigation leads to cooling effects on the cropland WFs in the growing season. Meanwhile, the daytime ΔLST on grassland WFs is higher in Dwa than in Dfa climate zones (Fig. S4 (a), (c)). This might be due to more water resources in the Dfa zone than in the Dwa zone, there are higher ΔLST on drier WFs, while the warming effects of WFs are lower in relatively moist areas (Fig. 4).

The wind turbine properties like hub height, rotor diameter, and rated power are key determinants that will decide the turbulence strength it creates and wind energy it removes, which in turn may affect the magnitude of ΔLST on WFs combined with the status of ABL stability (Fitch et al., 2013). To figure out the ΔLST magnitude affected by turbine properties, we analyze the linear relationships between the properties and ΔLST based on US Wind Turbines Dataset. The results show that there are no obvious dependencies of ΔLSTs on hub height, rotor diameter, and rated power (Fig. S5), this might be because ΔLST is also affected by the ABL stabilities and wind turbine operation periods in the consideration of turbulence strength. To achieve a more precise understanding of the impact of wind turbine properties on ΔLST, it may be necessary to integrate more accurate datasets on ABL stability and wind turbine operation.

4.4. Uncertainty and future work

In a previous study, the impacts of 319 WFs on local LSTs in the US indicated that the average daytime ΔLST is 0.01 °C, while the average nighttime ΔLST is 0.10 °C. The proportions of WFs with warming trends are 49.84 % and 61.13 % in the daytime and nighttime, respectively (Qin et al., 2022). However, in this study, the warming impacts in the daytime and nighttime are more obvious, at 0.080 °C and 0.191 °C, respectively, with proportions of 64.55 % and 90.91 %, in the US. Three major reasons might explain this phenomenon. First, the WFs considered by Qin et al. contained >25 turbines, while the number of turbines in the considered WFs exceeded 100 in this study. The large WFs on the Great Plains and Central Plains considered in the study of Qin et al. showed warming patterns similar to our results. However, the small WFs (with turbine numbers ⟨100) in other regions (e.g., the east coast or the Rocky Mountains) that were not picked in our study mostly showed cooling effects. Second, there was a difference in the study periods considered between the studies. The study period considered by Qin et al. for each WF was set up by defining the installation year and building a five-year window comprising two years before and after that specific year. The effect of the WFs was then calculated using those windows. However, the installation of a WF is a continuous process that can last for several years. For example, the installation period of a large WF with 304 turbines in Texas lasted from 2007 to 2015. Thus, the use of a five-year window might weaken the effect. By using the comparison strategy between the WFPs and the BUPs to calculate the LST impacts of the WFs (ΔLST), we can describe the relationship between ΔLST and the growing process of WFs (Fig. S6). Notably, in both the case of the grassland WF in Texas and the cropland WF in Indiana, we observe a transition in the ΔLST from a descending trend to an ascending trend along with the construction of the respective WFs. Third, regarding the WF area differences, Qin et al. defined turbine points as the WF area and calculated the mean LST of the WF via the mean value of the points. In comparison, the WF area considered in this study is established using the WFPs. Turbines are always distributed unevenly in a WF, and the influences of the turbines are not only concentrated on the bottom points of the turbines. Thus, the use of different WF area definitions might bring differences in the results.

DEM gaps between WFPs and BUPs might lead to ABL stability and plant species difference (Cuxart et al., 2000; Jones et al., 2003), and further interfere ΔLST in this study. To figure out whether WFs lead to obvious ΔLST in the absence of huge DEM gaps, we applied filters of WFs with δDEM of ±30 m, ±20 m, and ±10 m. It is shown in Fig. S7 that WF-induced ΔLST is significant in both daytime and nighttime where there are minor DEM gaps between WFPs and BUPs. It is obvious that most WFs are concentrated in both China and the US, while some others are located in faraway areas, which might lead to climate and terrain differences between the two groups. Thus, we made a comparison of WF-induced ΔLST between the concentrated and scattered WFs. Results indicate a lack of significant ΔLST differences between the concentrated and scattered WFs during the daytime and nighttime, with *p*-values of 0.39 and 0.78, respectively (Fig. S8). The influences of location on WF-induced ΔLST are probably not apparent based on remote sensing observations. To assess the potential impact of land cover changes on our study period from 2001 to 2018, we analyzed the distribution of grassland, cropland, and other land cover types within the WFPs and BUPs of all 186 WFs, and for China and the US, separately (Fig. S9). The results indicate that there have been minimal changes in cropland pixels, with a slight increase of 0.2 % from 2001 to 2018. The percentage of grassland pixels has also seen a modest increase of <1 %. Since there have been no significant land cover changes observed within the 186 WFs analyzed in this study, it is unlikely that land cover changes have a substantial impact on the ΔLST calculation.

In addition, when calculating the impacts of WFs on LSTs, more uncertainties could be brought by turbines and observations. First, the operation times of the studied turbines are unknown to us. The turbines start working when the wind speed reaches its cut-in speed and stop when the wind speed exceeds the cut-out speed to avoid mechanical damage (Fan and Zhu, 2019). With precise operation profile, we will be able to make obtain more accurate results of ΔLSTs. Second, the types and sizes of wind turbines differ among installation times and countries, causing differences in the turbulent kinetic energy sink and turbulence strength to arise (Chinese Wind Energy Association, 2019). Third, although studying WF impacts on LSTs using long-time-series remote sensing products is a suitable method, in situ measurements are still necessary because of the uncertainties inherent in remote sensing products. Fourth, the phenology and evapotranspiration strength vary among vegetation species (Béziat et al., 2013; Pauliukonis and Schneider, 2001), and the WF impacts on LSTs in vegetated areas could be better revealed when these species are confined. The boosted regression tree model utilized in this study explains the ΔLST at a cross-validation correlation level of 0.51. In the future, the model could be improved by considering additional variables and physical processes.

The Weather Research and Forecasting (WRF) model has been widely used to simulate the impacts of WFs (Miller and Keith, 2018; Vautard et al., 2014; Xia et al., 2017; Xia et al., 2019). With abundant observation evidence, the WRF parameterization and WF modeling process could be improved. The purpose of WF installation is to reduce greenhouse gas (GHG) emissions and mitigate global climate change; however, WFs also create local side effects (Zhou et al., 2012; Keith et al., 2004; Li et al., 2018). According to previous studies, apart from changing the local climate conditions, WFs further affect ecosystem dynamics and animal diversity (Dai et al., 2015; Marques et al., 2014; Smallwood and Thelander, 2008), which might undermine their sustainability in vulnerable ecosystems such as grasslands and plateaus. However, based on our analysis, when installed on well-managed croplands, WFs can even promote local evapotranspiration and have cooling effects on local LSTs during the growing season. Thus, installing wind turbines in such areas might provide clean energy and mitigate global GHG emissions while having minor local side effects.

5. Conclusion

In this study, we detected the impacts of WFs on local daytime and nighttime LSTs by considering 186 large grassland and cropland WFs in China and the US. We found that the warming impacts of WFs in the US are more pronounced than those in China, especially for cropland WFs. These divergences are probably controlled by the cooling effects of cropland WFs with irrigation. By using a boosted regression tree model, the heterogeneities in the impacts of WFs on LSTs are found to be contributed mainly by climate and terrain factors. The results suggest that when producing clean electricity and altering the large-scale land surface and ABL conditions during the rapid development of wind energy, the locations of future WFs could be optimized to minimize local side effects.

CRediT authorship contribution statement

Naijing Liu: Formal analysis, Investigation, Validation, Visualization, Writing – original draft. **Xiang Zhao:** Conceptualization, Supervision, Funding acquisition, Methodology, Writing – review & editing. **Xin Zhang:** Conceptualization, Data curation, Writing – review & editing. **Jiacheng Zhao:** Methodology, Writing – review & editing. **Haoyu Wang:** Writing – review & editing. **Donghai Wu:** Conceptualization, Formal analysis, Methodology, Validation, Visualization, Writing – original draft, Writing – review & editing.

Declaration of competing interest

The authors declare that they have no known competing financial interests or personal relationships that could have appeared to influence the work reported in this paper.

Data availability

Data will be made available on request.

Acknowledgments

This work is supported by National Key Research and Development Program of China (2022YFF1303401) and the National Natural Science Foundation of China (Grant No.42090012). Donghai Wu is funded by South China Botanical Garden, Chinese Academy of Sciences (Granted No: QNXM-202308, No. 2022B1111230001, and No. 2023000051).

Appendix A. Supplementary data

Supplementary data to this article can be found online at https://doi.org/10.1016/j.scitotenv.2023.167203.

References

Armstrong, A., Waldron, S., Whitaker, J., Ostle, N.J., 2014. Wind farm and solar park effects on plant-soil carbon cycling: uncertain impacts of changes in ground-level microclimate. Glob. Chang. Biol. 20 (6), 1699–1706. https://doi.org/10.1111/gcb.12437.

Beck, H.E., Zimmermann, N.E., McVicar, T.R., Vergopolan, N., Berg, A., Wood, E.F., 2018. Present and future Köppen-Geiger climate classification maps at 1-km resolution. Sci. Data 5 (1), 1–12.

Béziat, P., Rivalland, V., Tallec, T., Jarosz, N., Boulet, G., Gentine, P., Ceschia, E., 2013. Evaluation of a simple approach for crop evapotranspiration partitioning and analysis of the water budget distribution for several crop species. Agric. For. Meteorol. 177, 46–56.

Ceccato, P., Flasse, S., Tarantola, S., Jacquemoud, S., Grégoire, J.-M., 2001. Detecting vegetation leaf water content using reflectance in the optical domain. Remote Sens. Environ. 77 (1), 22–33.

Chinese Wind Energy Association, 2019. China Wind Power Industry Mapping 2018.

Cuxart, J., Yagüe, C., Morales, G., Terradellas, E., Orbe, J., Calvo, J., Fernández, A., Soler, M., Infante, C., Buenestado, P., others, 2000. Stable atmospheric boundary-layer experiment in Spain (SABLES 98): a report. Bound.-Layer Meteorol. 96, 337–370.

Dai, K., Bergot, A., Liang, C., Xiang, W.-N., Huang, Z., 2015. Environmental issues associated with wind energy – a review. Renew. Energy 75, 911–921. https://doi.org/10.1016/j.renene.2014.10.074.

De Keersmaecker, W., Lhermitte, S., Tits, L., Honnay, O., Somers, B., Coppin, P., 2015. A model quantifying global vegetation resistance and resilience to short-term climate anomalies and their relationship with vegetation cover. Glob. Ecol. Biogeogr. 24 (5), 539–548.

Didan, K., 2015. MOD13A1 MODIS/Terra Vegetation Indices 16-Day L3 Global 500m SIN Grid V006. NASA EOSDIS Land Processes DAAC, 10.

Fan, Z., Zhu, C., 2019. The optimization and the application for the wind turbine power-wind speed curve. Renew. Energy 140, 52–61.

Fitch, A.C., Olson, J.B., Lundquist, J.K., 2013. Parameterization of wind farms in climate models. J. Clim. 26 (17), 6439–6458.

Freund, Y., Schapire, R.E., 1997. A decision-theoretic generalization of on-line learning and an application to boosting. J. Comput. Syst. Sci. 55 (1), 119–139.

Gorelick, N., Hancher, M., Dixon, M., Ilyushchenko, S., Thau, D., Moore, R., 2017. Google earth engine: planetary-scale geospatial analysis for everyone. Remote Sens. Environ. 202, 18–27.

He, Y., Lee, E., Mankin, J.S., 2020. Seasonal tropospheric cooling in Northeast China associated with cropland expansion. Environ. Res. Lett. 15 (3), 034032 https://doi.org/10.1088/1748-9326/ab6616.

International Energy Agency, 2021. Wind Power – Analysis. IEA. https://www.iea.org/reports/wind-power (accessed 13 Sep 2022).

Jarvis, A., Reuter, H.I., Nelson, A., Guevara, E., et al., 2008. Hole-filled SRTM for the Globe Version 4, Available From the CGIAR-CSI SRTM 90m Database.

Jones, J.I., Li, W., Maberly, S.C., 2003. Area, altitude and aquatic plant diversity. Ecography 26 (4), 411–420.

Jung, M., Reichstein, M., Ciais, P., Seneviratne, S.I., Sheffield, J., Goulden, M.L., Bonan, G., Cescatti, A., Chen, J., De Jeu, R., et al., 2010. Recent decline in the global land evapotranspiration trend due to limited moisture supply. Nature 467 (7318), 951–954.

Keith, D.W., DeCarolis, J.F., Denkenberger, D.C., Lenschow, D.H., Malyshev, S.L., Pacala, S., Rasch, P.J., 2004. The influence of large-scale wind power on global climate. Proc. Natl. Acad. Sci. 101 (46), 16115–16120. https://doi.org/10.1073/pnas.0406930101.

Kimm, H., Guan, K., Gentine, P., Wu, J., Bernacchi, C.J., Sulman, B.N., Griffis, T.J., Lin, C., 2020. Redefining droughts for the US Corn Belt: the dominant role of atmospheric vapor pressure deficit over soil moisture in regulating stomatal behavior of maize and soybean. Agric. For. Meteorol. 287, 107930.

Li, Y., Kalnay, E., Motesharrei, S., Rivas, J., Kucharski, F., Kirk-Davidoff, D., Bach, E., Zeng, N., 2018. Climate model shows large-scale wind and solar farms in the Sahara increase rain and vegetation. Science 361 (6406), 1019–1022. https://doi.org/10.1126/science.aar5629.

Liu, N., Zhao, X., Zhang, X., Zhao, J., Wang, H., Wu, D., 2022. Heterogeneous warming impacts of desert wind farms on land surface temperature and their potential drivers in Northern China. Environ. Res. Commun. 4, 105006 https://doi.org/10.1088/2515-7620/ac9bd7.

Ljungqvist, F.C., Krusic, P.J., Brattström, G., Sundqvist, H.S., 2012. Northern hemisphere temperature patterns in the last 12 centuries. Clim. Past 8 (1), 227–249.

Lobell, D.B., Bonfils, C.J., Kueppers, L.M., Snyder, M.A., 2008. Irrigation cooling effect on temperature and heat index extremes. Geophys. Res. Lett. 35(9).

Lundquist, J.K., DuVivier, K.K., Kaffine, D., Tomaszewski, J.M., 2019. Costs and consequences of wind turbine wake effects arising from uncoordinated wind energy development. Nat. Energy 4 (1), 26–34.

Malek, E., 1992. Night-time evapotranspiration vs. daytime and 24h evapotranspiration. J. Hydrol. 138 (1–2), 119–129.

Marques, A.T., Batalha, H., Rodrigues, S., Costa, H., Pereira, M.J.R., Fonseca, C., Mascarenhas, M., Bernardino, J., 2014. Understanding bird collisions at wind farms: an updated review on the causes and possible mitigation strategies. Biol. Conserv. 179, 40–52.

McGarigal, K., 1995. FRAGSTATS: Spatial Pattern Analysis Program for Quantifying Landscape Structure. US Department of Agriculture, Forest Service, Pacific Northwest Research Station.

Miller, L.M., Keith, D.W., 2018. Climatic impacts of wind power. Joule 2 (12), 2618–2632. https://doi.org/10.1016/j.joule.2018.09.009.

Muñoz-Sabater, J., Dutra, E., Agustí-Panareda, A., Albergel, C., Arduini, G., Balsamo, G., Boussetta, S., Choulga, M., Harrigan, S., Hersbach, H., 2021. Others. ERA5-land: a state-of-the-art global reanalysis dataset for land applications. Earth Syst. Sci. Data 13 (9), 4349–4383.

Oke, T.R., 1973. City size and the urban heat island. Atmos. Environ. 7 (8), 769–779.

Osakabe, Y., Osakabe, K., Shinozaki, K., Tran, L.-S.P., 2014. Response of plants to water stress. Front. Plant Sci. 5, 86.

Pallas Jr., J., Michel, B.E., Harris, D.G., 1967. Photosynthesis, transpiration, leaf temperature, and stomatal activity of cotton plants under varying water potentials. Plant Physiol. 42 (1), 76–88.
Pauliukonis, N., Schneider, R., 2001. Temporal patterns in evapotranspiration from lysimeters with three common wetland plant species in the eastern United States. Aquat. Bot. 71 (1), 35–46.
Pryor, S.C., Barthelmie, R.J., Shepherd, T.J., 2018. The influence of real-world wind turbine deployments on local to mesoscale climate. J. Geophys. Res. Atmos. 123 (11), 5804–5826. https://doi.org/10.1029/2017JD028114.
Purdy, A.J., Fisher, J.B., Goulden, M.L., Colliander, A., Halverson, G., Tu, K., Famiglietti, J.S., 2018. SMAP soil moisture improves global evapotranspiration. Remote Sens. Environ. 219, 1–14.
Qin, Y., Li, Y., Xu, R., Hou, C., Armstrong, A., Bach, E., Wang, Y., Fu, B., 2022. Impacts of 319 wind farms on surface temperature and vegetation in the United States. Environ. Res. Lett. 17 (2), 024026 https://doi.org/10.1088/1748-9326/ac49ba.
Ragheb, M., Ragheb, A.M., 2011. Wind turbines theory-the betz equation and optimal rotor tip speed ratio. Fundament. Adv. Top. Wind Power 1 (1), 19–38.
Rand, J.T., Kramer, L.A., Garrity, C.P., Hoen, B.D., Diffendorfer, J.E., Hunt, H.E., Spears, M., 2020. A continuously updated, geospatially rectified database of utility-scale wind turbines in the United States. Sci. Data 7 (1), 1–12.
Redmon, J., Divvala, S., Girshick, R., Farhadi, A., 2016. You only look once: unified, real-time object detection. In: 2016 IEEE Conference on Computer Vision and Pattern Recognition (CVPR). IEEE: Las Vegas, NV, USA, pp. 779–788.
Roy, S.B., Traiteur, J.J., 2010. Impacts of wind farms on surface air temperatures. Proc. Natl. Acad. Sci. 107 (42), 17899–17904.
Running, S., Zhao, M., 2019. MOD17A3HGF MODIS/Terra Net Primary Production Gap-Filled Yearly L4 Global 500 m SIN Grid V006. NASA EOSDIS Land Processes DAAC.
Running S, Mu Q, Zhao M. MOD17A2H MODIS/Terra Gross Primary Productivity 8-Day L4 Global 500m SIN Grid V006. 2015. doi:https://doi.org/10.5067/MODIS/MOD17A2H.006 (accessed 21 Apr 2021).
Running, S., Mu, Q., Zhao, M., 2017. MOD16A2 MODIS/Terra Net Evapotranspiration 8-Day L4 Global 500m SIN Grid V006. https://doi.org/10.5067/MODIS/MOD16A2.006 (accessed 21 Apr 2021).
Seneviratne, S.I., Corti, T., Davin, E.L., Hirschi, M., Jaeger, E.B., Lehner, I., Orlowsky, B., Teuling, A.J., 2010. Investigating soil moisture–climate interactions in a changing climate: a review. Earth Sci. Rev. 99 (3–4), 125–161.
Slawsky, L., Zhou, L., Roy, S., Xia, G., Vuille, M., Harris, R., 2015. Observed thermal impacts of wind farms over Northern Illinois. Sensors 15 (7), 14981–15005. https://doi.org/10.3390/s150714981.
Smallwood, K.S., Thelander, C., 2008. Bird mortality in the Altamont pass wind resource area, California. J. Wildl. Manag. 72 (1), 215–223.
Sun, Q., Miao, C., Duan, Q., Ashouri, H., Sorooshian, S., Hsu, K.-L., 2018. A review of global precipitation data sets: data sources, estimation, and intercomparisons. Rev. Geophys. 56 (1), 79–107.
Tabassum-Abbasi, Premalatha M., Abbasi, T., Abbasi, S.A., 2014. Wind energy: increasing deployment, rising environmental concerns. Renew. Sust. Energ. Rev. 31, 270–288. https://doi.org/10.1016/j.rser.2013.11.019.
Tang, B., Wu, D., Zhao, X., Zhou, T., Zhao, W., Wei, H., 2017. The observed impacts of wind farms on local vegetation growth in northern China. Remote Sens. 9 (4), 332.
Teluguntla, P., Thenkabail, P.S., Xiong, J., Gumma, M.K., Giri, C., Milesi, C., Ozdogan, M., Congalton, R., Tilton, J., Sankey, T.T., et al., 2015. Global Cropland Area Database (GCAD) Derived From Remote Sensing in Support of Food Security in the Twenty-first Century: Current Achievements and Future Possibilities.
Torres, R., Snoeij, P., Geudtner, D., Bibby, D., Davidson, M., Attema, E., Potin, P., Rommen, B., Floury, N., Brown, M., others, 2012. GMES sentinel-1 mission. Remote Sens. Environ. 120, 9–24.
Vautard, R., Thais, F., Tobin, I., Bréon, F.-M., de Lavergne, J.-G.D., Colette, A., Yiou, P., Ruti, P.M., 2014. Regional climate model simulations indicate limited climatic impacts by operational and planned European wind farms. Nat. Commun. 5 (1), 3196. https://doi.org/10.1038/ncomms4196.
Veers, P., Dykes, K., Lantz, E., Barth, S., Bottasso, C.L., Carlson, O., Clifton, A., Green, J., Green, P., Holttinen, H., et al., 2019. Grand challenges in the science of wind energy. Science 366 (6464).
Wan, Z., Hook, S., Hulley, G., 2015. MOD11A1 MODIS/Terra Land Surface Temperature/Emissivity Daily L3 Global 1km SIN Grid V006. https://doi.org/10.5067/MODIS/MOD11A1.006 (accessed 21 Apr 2021).
Wang, S., Wang, S., 2015. Impacts of wind energy on environment: a review. Renew. Sust. Energ. Rev. 49, 437–443. https://doi.org/10.1016/j.rser.2015.04.137.
World Wind Energy Association, 2019. Wind Power Capacity Worldwide Reaches 597 GW, 50,1 GW Added in 2018. https://wwindea.org/wind-power-capacity-worldwide-reaches-600-gw-539-gw-added-in-2018/.
Wu, S., Archer, C.L., 2021. Near-ground effects of wind turbines: observations and physical mechanisms. Mon. Weather Rev. 149 (3), 879–898.
Wu, X., Zhang, L., Zhao, C., Gegen, T., Zheng, C., Shi, X., Geng, J., Letu, H., 2019. Satellite-based assessment of local environment change by wind farms in China. Earth Space Sci. 6 (6), 947–958. https://doi.org/10.1029/2019EA000628.
Xia, G., Zhou, L., Freedman, J.M., Roy, S.B., Harris, R.A., Cervarich, M.C., 2016. A case study of effects of atmospheric boundary layer turbulence, wind speed, and stability on wind farm induced temperature changes using observations from a field campaign. Clim. Dyn. 46 (7–8), 2179–2196.
Xia, G., Cervarich, M.C., Roy, S.B., Zhou, L., Minder, J.R., Jimenez, P.A., Freedman, J.M., 2017. Simulating impacts of real-world wind farms on land surface temperature using the WRF model: validation with observations. Mon. Weather Rev. 145 (12), 4813–4836. https://doi.org/10.1175/MWR-D-16-0401.1.
Xia, G., Zhou, L., Minder, J.R., Fovell, R.G., Jimenez, P.A., 2019. Simulating impacts of real-world wind farms on land surface temperature using the WRF model: physical mechanisms. Clim. Dyn. 53 (3–4), 1723–1739. https://doi.org/10.1007/s00382-019-04725-0.
Yao, Y., Liang, S., Li, X., Chen, J., Liu, S., Jia, K., Zhang, X., Xiao, Z., Fisher, J.B., Mu, Q., Pan, M., Liu, M., Cheng, J., Jiang, B., Xie, X., Grünwald, T., Bernhofer, C., Roupsard, O., 2017. Improving global terrestrial evapotranspiration estimation using support vector machine by integrating three process-based algorithms. Agric. For. Meteorol. 242, 55–74. https://doi.org/10.1016/j.agrformet.2017.04.011.
Yin, L., Feng, X., Fu, B., Chen, Y., Wang, X., Tao, F., 2020. Irrigation water consumption of irrigated cropland and its dominant factor in China from 1982 to 2015. Adv. Water Resour. 143, 103661.
Zhang, X., Han, L., Han, L., Zhu, L., 2020. How well do deep learning-based methods for land cover classification and object detection perform on high resolution remote sensing imagery? Remote Sens. 12 (3), 417.
Zhou, L., Tian, Y., Baidya Roy, S., Thorncroft, C., Bosart, L.F., Hu, Y., 2012. Impacts of wind farms on land surface temperature. Nat. Clim. Chang. 2 (7), 539–543. https://doi.org/10.1038/nclimate1505.
Zhou, L., Tian, Y., Chen, H., Dai, Y., Harris, R.A., 2013. Effects of topography on assessing wind farm impacts using MODIS data. Earth Interact. 17 (13), 1–18. https://doi.org/10.1175/2012EI000510.1.
Zhou, L., Baidya Roy, S., Xia, G., 2020. Weather, climatic and ecological impacts of onshore wind farms. In: Reference Module in Earth Systems and Environmental Sciences. Elsevier (p B9780128197271001000).